9-18-2015

Emergence of Room-Temperature Ferroelectricity at Reduced Dimensions

D. A. Tenne

Boise State University

Emergence of Room-Temperature Ferroelectricity at Reduced Dimensions

D. Lee[1], H. Lu[2], Y. Gu[3], S.-Y. Choi[4], S.-D. Li[5], S. Ryu[1], T. R. Paudel[2], K. Song[6], E. Mikheev[7], S. Lee[1], S. Stemmer[7], D. A. Tenne[8], S. H. Oh[6], E. Y. Tsymbal[2], X. Wu[5], L.-Q. Chen[3], A. Gruverman[2]*, C. B. Eom[1]*

[1]Department of Materials Science and Engineering, University of Wisconsin–Madison, Madison, Wisconsin 53706, USA.

[2]Department of Physics and Astronomy & Nebraska Center for Materials and Nanoscience, University of Nebraska, Lincoln–Nebraska, Nebraska 68588, USA.

[3]Department of Materials Science and Engineering, Pennsylvania State University, University Park, Pennsylvania 16802 USA.

[4]Advanced Characterization and Analysis Group, Korea Institute of Materials Science, Changwon 641-831, Korea.

[5]Department of Physics, Temple University, Philadelphia, Pennsylvania 19122, USA.

[6]Department of Materials Science and Engineering, Pohang University of Science and Technology, Pohang 790-784, Korea.

[7]Materials Department, University of California–Santa Barbara, Santa Barbara, California 93106-5050, USA.

[8]Department of Physics, Boise State University, Boise, Idaho 83725-1570, USA.

*Correspondence to: agruverman2@unl.edu (A.G.); eom@engr.wisc.edu (C.B.E.)

The enhancement of the functional properties of materials at reduced dimensions is crucial for continuous advancements in nanoelectronic applications. Here, we report that the scale reduction leads to the emergence of an important functional property – ferroelectricity, challenging the long-standing notion that ferroelectricity is inevitably suppressed at the scale of a few nanometers. A combination of theoretical calculations, electrical measurements, and structural analyses provides evidence of room-temperature ferroelectricity in strain-free epitaxial nanometer-thick films of otherwise non-ferroelectric $SrTiO_3$. We show that electrically-induced alignment of naturally existing polar nanoregions is responsible for the appearance of a stable net ferroelectric polarization in these films. This finding can be useful for the development of low-dimensional material systems with enhanced functional properties relevant to emerging nanoelectronic devices.

Low-dimensional ferroelectric structures hold a great potential for scientific and technological endeavors (*1*). Reducing size while retaining ferroelectric properties enables an increase in the storage capacity of non-volatile ferroelectric memories (*2*), exploration of diverse nanoelectronic functions (*3–7*), and discovery of exotic physical phenomena (*8*, *9*). However, maintaining the ferroelectricity in low-dimensional structures, such as ultrathin films, has been hampered by depolarization effects (*10–12*), which arise from the uncompensated charges at the interface. The strong scaling effect seems to inevitably suppress ferroelectricity and its functions below a critical dimension (*10–13*). A recent theoretical work suggested an intriguing concept for reversibly enhancing ferroelectricity in ultrathin ferroelectric capacitors via the tailoring of chemical bonds at the metal/oxide interface (*14*), but this mechanism has not yet been experimentally confirmed.

Here, we demonstrate a different mechanism, which enables enhancement of ferroelectricity as the thickness of the system is decreased. In our approach, we utilize naturally existing polar nanoregions (PNRs), i.e., local nanometer-sized polar clusters, in an archetype dielectric material with perovskite structure - $SrTiO_3$. PNRs are generally believed to arise from local nanoscale inhomogeneities (e.g., chemical or structural disorder) (*15*, *16*), which exist in every material (*17*). For example, Sr vacancies are intrinsic point defects in $SrTiO_3$ due to their small formation energy (*18*, *19*), comparable to that of oxygen vacancies, which are likely to act as a natural source of PNRs (Fig. 1A) (*20*, *21*). It has been previously shown (*20*) that relatively thick (tens of nanometers) films of $SrTiO_3$ exhibit relaxor behavior at low temperatures due to the presence of the PNRs. Here, we demonstrate that electrically-induced alignment and stabilization of PNRs in nanometer-thick $SrTiO_3$ films results in the emergence of net ferroelectric polarization at room temperature.

Calculations predict that when $SrTiO_3$ is deficient in Sr, antisite Ti defects could instantaneously form and generate local dipole moments by an off-centering displacement (Fig. 1C) (*22*). Our first-principles density-functional theory (DFT) modeling (*23*) shows that the energy gain due to this Ti off-centering is as large as ~0.5 eV, originating from structural distortion driven by an ionic radii difference between Ti^{2+} (0.86 Å) and Sr^{2+} (1.44 Å). A local polarization profile around the antisite Ti atom (Fig. 1D) indicates that the off-centered antisite Ti atom induces a large local polarization in its residing unit cell and coherently polarizes the surrounding region. The polarization switchability follows from a calculated energy barrier of about 0.1 eV between the polarization states (Fig. 1E), comparable to a double-well potential barrier in conventional ferroelectric materials (*24*). Thus, although pure bulk $SrTiO_3$ is centrosymmetric and nonpolar (*25*), the PNRs of nanometer characteristic size can naturally form due to the intrinsic Sr deficiency in $SrTiO_3$.

We have previously observed Sr deficiency and associated PNRs even in nominally stoichiometric $SrTiO_3$ bulk single crystals and films (*20*, *21*). These small-sized PNRs, however, do not necessarily generate ferroelectricity. When the film thickness t is much larger than the average PNR size ξ (Fig. 1A), PNRs are isolated in an insulating matrix. The depolarization field E_d in PNRs cannot be effectively screened, and thus destabilizes the polarization of PNRs. On the other hand, as t is decreased, the PNRs can play a vital role in the emergence of ferroelectricity (Fig. 1B). When t becomes comparable to or smaller than ξ, the electrical boundary conditions for PNRs drastically change as their interfaces come in contact with metallic electrodes and/or become exposed to surface adsorbates. The external charges screen the E_d by compensating for the polarization charge, and thus can allow a switchable and stable polarization in PNRs. Such dimensional engineering of polarization stability in PNRs would

provide an unconventional way to create and enhance ferroelectricity at reduced dimensions, distinct from methods such as strain (*26–28*) and interface (*13*, *14*) engineering.

Phase-field simulations were used to model polarization in a representative PNR region with a dimension of 7.5 nm embedded in the $SrTiO_3$ film (*23*). The thickness of the $SrTiO_3$ film in the simulations was varied within the range of 64 unit cells (uc) (or 25 nm) to 8 uc (3.2 nm) (*23*). External charges were introduced on the top and bottom $SrTiO_3$ interfaces, and the stability of the PNR polarization after poling by an external electric field was investigated. After the electric field was removed and the system was relaxed to equilibrium, the remnant polarization was evaluated over the whole $SrTiO_3$ film (i.e., by the average over the volume). It was found that a decrease in the $SrTiO_3$ thickness not only results in a more stable polar state, but also greatly enhances the remnant polarization of the system (Fig. 1F). This implies a possible creation and enhancement of ferroelectricity at the reduced scale via the PNR-related mechanism.

We experimentally tested these theoretical predictions in strain-free (001) single crystal $SrTiO_3$ films (*23*), grown on a (001) $SrTiO_3$ substrate with a single crystal conductive oxide $SrRuO_3$ bottom electrode (*29*). Film thickness was atomically controlled in the range of 120 uc to 6 uc (fig. S1). The nominally stoichiometric films had a normal unit-cell volume, almost the same as that of the substrate, indicating that the films were nearly free of excessive point defects (fig. S2). Only minute amounts of Sr deficiency (~1 atomic % at most) were present, possibly due to small formation energy (figs. S3 and S4) (*18*, *19*). As mentioned above, Sr deficiency can naturally generate PNRs (Figs. 1, C–E) without compromising crystalline quality of the film, according to the theoretical calculations. Second harmonic generation and Raman spectroscopy measurements provide further evidence of the PNR formation in our $SrTiO_3$ films (*20*, *21*) with a nonpolar-to-polar transition at ~400 K (fig. S3).

4

To directly visualize the PNRs in our films, we used aberration-corrected scanning transmission electron microscopy (STEM) with high-angle annular-dark-field (HAADF) and annular-bright-field (ABF) techniques (*30*, *31*). We detected the atomic positions of Sr, Ti, and O in the 12-uc-thick film from the ABF-STEM image (Fig. 2A) and the simultaneously obtained HAADF-STEM image (*23*), which allowed us to determine the polar atomic displacements. The magnitude of atomic displacements in polar regions (denoted by (i) in Fig. 2A) was as large as ~0.1 Å (comparable with that of conventional ferroelectric $BaTiO_3$ (*24*)), but was negligible in other regions (denoted by (ii) in Fig. 2A). The measured magnitude of atomic displacements is comparable to the calculated average magnitude (~0.06 Å) of atomic displacements in our theoretical model (Fig. 1C). Polarization maps obtained from the Ti and O displacements (*23*) indicate the presence of PNRs with a size of a few nanometers, whereas no clear polarization pattern is observed in the $SrRuO_3$ region (Fig. 2B). PNRs have a downward polarization state in the as-grown film, consistent with ferroelectric domain measurements by piezo-force microscopy (PFM) (fig. S6). Following the theoretical modeling and calculations (Fig. 1, B and F), these PNRs may enable ferroelectricity in ultrathin $SrTiO_3$ films, although they cannot generate a macroscopic net polarization in bulk or thick films.

Using a PFM approach, we found that the stable and switchable polarization could indeed be realized at room temperature in ultrathin $SrTiO_3$ films (Fig. 3) (*23*). Bipolar domain patterns, similar to those generated in conventional ferroelectric $BaTiO_3$ films (*5*, *32*), have been created in the $SrTiO_3$ films with a thickness of less than 60 uc by scanning the film surface with an electrically-biased PFM tip. Bulk-like 120-uc-thick $SrTiO_3$ film did not show any PFM contrast after poling, consistent with the notion that PNRs are effective only in the thinnest films. The stability of the written domain patterns was thickness-dependent: whereas the PFM contrast

5

disappeared within a few minutes in the 60-uc-thick film, the bipolar domain patterns were distinct and stable for several hours or more in thinner films (e.g., 12-uc-thick film) that exhibited a polarization stability as good as that of ferroelectric 12-uc-thick $BaTiO_3$ films (fig. S8). The PFM result demonstrates that the switchable and stable polarization, which is the signature of ferroelectricity, emerges at room temperature in ultrathin films of otherwise non-ferroelectric $SrTiO_3$.

Further evidence for room-temperature ferroelectricity in ultrathin $SrTiO_3$ films was obtained directly from polarization hysteresis (P–E) loops. The 24-uc-thick $SrTiO_3$ films showed a clear polarization hysteresis with nonzero remnant polarization, whereas bulk-like 120-uc-thick $SrTiO_3$ films showed no hysteresis with a paraelectric-like behavior (Fig. 4A). The measured P–E curves included a strong nonlinear dielectric contribution. To eliminate this response and to enable a more accurate measurement, we used the double-wave method (*33*), giving a switched polarization $\Delta P = P^+ - P^-$ of ~1.4 $\mu C/cm^2$ for the 24-uc-thick $SrTiO_3$ films, but $\Delta P \approx 0$ for the 120-uc-thick films (Fig. 4B). Considering the low density of PNRs in our films, the measured ΔP value seems reasonable, but we believe that it can be increased by interfacial engineering for more efficient charge compensation (*13*, *14*). Our PFM and hysteresis measurements unambiguously confirm room-temperature ferroelectricity in ultrathin $SrTiO_3$ films as well as the enhancement of ferroelectricity at the nanoscale range in agreement with the theoretical predictions (Fig. 1).

This study demonstrates that size reduction does not necessarily lead to the deterioration of ferroelectric properties, but in fact could enhance them. Although this mechanism might be limited to the ferroelectrics with a relatively low value of polarization and relaxors, it provides a path toward devices with reduced dimensions where ferroelectricity is coupled to other

functional properties, such as two-dimensional conductivity (*34*), superconductivity (*35*), and magnetism (*36*). In particular, we envision non-volatile devices with ferroelectric polarization controlling interfacial carrier concentrations. Not limited to $SrTiO_3$, our approach can be applied to other perovskite dielectrics (*37*) in which PNRs are controlled by defect engineering, as well as artificially layered superlattices (*38*, *39*), where PNRs can influence multiple interfaces.

References and Notes:

1. C. H. Ahn, K. M. Rabe, J.-M. Triscone, Ferroelectricity at the nanoscale: local polarization in oxide thin films and heterostructures. *Science* **303**, 488–491 (2004).

2. J. F. Scott, C. A. Paz de Araujo, Ferroelectric memories. *Science* **246**, 1400–1405 (1989).

3. M. Y. Zhuravlev, R. F. Sabirianov, S. S. Jaswal, E. Y. Tsymbal, Giant electroresistance in ferroelectric tunnel junctions. *Phys. Rev. Lett.* **94**, 246802 (2005).

4. V. Garcia *et al.*, Giant tunnel electroresistance for non-destructive readout of ferroelectric states. *Nature* **460**, 81–84 (2009).

5. A. Gruverman *et al.*, Tunneling electroresistance effect in ferroelectric tunnel junctions at the nanoscale. *Nano Lett.* **9**, 3539−3543 (2009).

6. V. Garcia *et al.*, Ferroelectric control of spin polarization. *Science* **327**, 1106–1110 (2010).

7. D. Pantel, S. Goetze, D. Hesse, M. Alexe, Reversible electrical switching of spin polarization in multiferroic tunnel junctions. *Nat. Mater.* **11**, 289–293 (2012).

8. E. Durgun, P. Ghosez, R. Shaltaf, X. Gonze, J.-Y. Raty, Polarization vortices in germanium telluride nanoplatelets: A theoretical study. *Phys. Rev. Lett.* **103**, 247601 (2009).

9. J. Mannhart, D. G. Schlom, Oxide interfaces—an opportunity for electronics. *Science* **327**, 1607–1611 (2010).

10. W. L. Zhong, Y. G. Wang, P. L. Zhang, B. D. Qu, Phenomenological study of the size effect on phase transitions in ferroelectric particles. *Phys. Rev. B* **50**, 698–703 (1994).

11. J. Junquera, Ph. Ghosez, Critical thickness for ferroelectricity in perovskite ultrathin films. *Nature* **422**, 506–509 (2003).

12. C. Lichtensteiger, J.-M. Triscone, J. Junquera, Ph. Ghosez, Ferroelectricity and tetragonality in ultrathin $PbTiO_3$ films. *Phys. Rev. Lett.* **94**, 047603 (2005).

13. H. Lu *et al.*, Enhancement of ferroelectric polarization stability by interface engineering. *Adv. Mater.* **24**, 1209–1216 (2012).

14. M. Stengel, D. Vanderbilt, N. A. Spaldin, Enhancement of ferroelectricity at metal–oxide interfaces. *Nat. Mater.* **8**, 392–397 (2009).

15. G. Burns, F. H. Dacol, Crystalline ferroelectrics with glassy polarization behavior. *Phys. Rev. B* **28**, 2527–2530 (1983).

16. L. E. Cross, Relaxor ferroelectrics. *Ferroelectrics* **76**, 241–267 (1987).

17. N. W. Ashcroft, N. D. Mermin, *Solid State Physics* (Holt, Rinehart and Winston, New York, 1976).

18. K. R. Udayakumar, A. N. Cormack, Non-stoichiometry in alkaline earth excess alkaline earth titanate. *J. Phys. Chem. Solids* **50**, 55–60 (1989).

19. B. Liu *et al.*, Composition dependent intrinsic defect structures in $SrTiO_3$. *Phys. Chem. Chem. Solids* **16**, 15590–15596 (2014).

20. H. W. Jang *et al.*, Ferroelectricity in strain-free $SrTiO_3$ thin films. *Phys. Rev. Lett.* **104**, 197601 (2010).

21. D. A. Tenne *et al.*, Ferroelectricity in nonstoichiometric SrTiO₃ films studied by ultraviolet Raman spectroscopy. *Appl. Phys. Lett.* **97**, 142901 (2010).

22. M. Choi, F. Oba, I. Tanaka, Role of Ti antisitelike defects in SrTiO₃. *Phys. Rev. Lett.* **103**, 185502 (2009).

23. Supplementary materials are available on *Science* Online.

24. R. E. Cohen, Origin of ferroelectricity in perovskite oxides. *Nature* **358**, 136–138 (1992).

25. K. A. Müller, H. Bukard, SrTiO₃: An intrinsic quantum paraelectric below 4 K. *Phys. Rev. B* **19**, 3593–3602 (1979).

26. J. H. Haeni *et al.*, Room-temperature ferroelectricity in strained SrTiO₃. *Nature* **430**, 758–761 (2004).

27. M. P. Warusawithana *et al.*, A ferroelectric oxide made directly on silicon. *Science* **324**, 367–370 (2009).

28. K. J. Choi *et al.*, Enhancement of ferroelectricity in strained BaTiO₃ thin films. *Science* **306**, 1005–1009 (2004).

29. C. B. Eom *et al.*, Single-crystal epitaxial thin films of the isotropic metallic oxides $Sr_{1-x}Ca_xRuO_3$. *Science* **258**, 1766–1769 (1992).

30. K. W. Urban, Studying atomic structures by aberration-corrected transmission electron microscopy. *Science* **321**, 506–510 (2008).

31. R. Ishikawa *et al.*, Direct imaging of hydrogen-atom columns in a crystal by annular bright-field electron microscopy. *Nat. Mater.* **10**, 278–281 (2011).

32. H. Lu *et al.*, Mechanical writing of ferroelectric polarization. *Science* **336**, 59–61 (2012).

33. J. F. Scott *et al.*, Switching kinetics of lead zirconate titanate submicron thin-film memories. *J. Appl. Phys.* **64**, 787–792 (1988).

34. A. Ohtomo, H. Y. Hwang, A high-mobility electron gas at the LaAlO₃/SrTiO₃ heterointerface. *Nature* **427**, 423–426 (2004).

35. N. Reyren *et al.*, Superconducting interfaces between insulating oxides. *Science* **317**, 1196–1199 (2007).

36. A. Brinkman *et al.*, Magnetic effects at the interface between non-magnetic oxides. *Nat. Mater.* **6**, 493–496 (2007).

37. U. Bianchi, J. Dec, W. Kleemann, J. G. Bednorz, Cluster and domain-state dynamics of ferroelectric $Sr_{1-x}Ca_xTiO_3$ ($x = 0.007$). *Phys. Rev. B* **51**, 8737–8746 (1995).

38. D. A. Tenne *et al.*, Probing nanoscale ferroelectricity by ultraviolet Raman spectroscopy. *Science* **313**, 1614–1616 (2006).

39. A. T. Bollinger *et al.*, Superconductor-insulator transition in $La_{2-x}Sr_xCuO_4$ at the pair quantum resistance. *Nature* **472**, 458–460 (2011).

40. T. Ohnishi, K. Shibuya, T. Yamamoto, M. Lippmaa, Defects and transport in complex oxide thin films. *J. Appl. Phys.* **103**, 103703 (2008).

41. J. Son *et al.*, Epitaxial SrTiO$_3$ films with electron mobilities exceeding 30,000 cm^2 V^{-1} s^{-1}. *Nat. Mater.* **9**, 482–484 (2010).

42. C.-L. Jia *et al.*, Unit-cell scale mapping of ferroelectricity and tetragonality in epitaxial ultrathin ferroelectric films. *Nat. Mater.* **6**, 64–69 (2007).

43. J. P. Perdew, K. Burke, M. Ernzerhof, Generalized gradient approximation made simple. *Phys. Rev. Lett.* **77**, 3865–3868(1996).

44. J. P. Perdew *et al.*, Restoring the density-gradient expansion for exchange in solids and surfaces. *Phys. Rev. Lett.* **100**, 136406 (2008).

45. J. D. Perkins *et al.*, Inverse design approach to hole doping in ternary oxides: Enhancing *p*-type conductivity in cobalt oxide spinels. *Phys. Rev. B* **84**, 205207 (2011).

46. R. D. King-Smith, D. Vanderbilt, *Phys. Rev. B* **47**, 1651–1654 (1993).

47. R. Resta, *Rev. Mod. Phys.* **66**, 899–915 (1994).

48. L. Q. Chen, J. Shen, Applications of semi-implicit Fourier-spectral method to phase field equations. *Comput. Phys. Commun.* **108**, 147–158 (1998).

49. Y. L. Li *et al.*, Phase transitions and domain structures in strained pseudocubic (100) SrTiO$_3$ thin films. *Phys. Rev. B* **73**, 184112 (2006).

50. Y. L. Li, S. Y. Hu, Z. K. Liu, L. Q. Chen, Effect of substrate constraint on the stability and evolution of ferroelectric domain structures in thin films. *Acta Mater.* **50**, 395–411 (2002).

51. A. G. Khachaturyan, *Theory of Structural Transformations in Solids* (DOVER PUBLICATIONS INC. Mineola, New York, 2008).

52. Y. L. Li, S. Y. Hu, Z. K. Liu, L. Q. Chen, Effect of electrical boundary conditions on ferroelectric domain structures in thin films. *Appl. Phys. Lett.* **81**, 427–429 (2002).

53. R. I. Eglitis, D. Vanderbilt, First-principles calculations of atomic and electronic structure of SrTiO$_3$ (001) and (011) surfaces. *Phys. Rev. B* **77**, 195408 (2008).
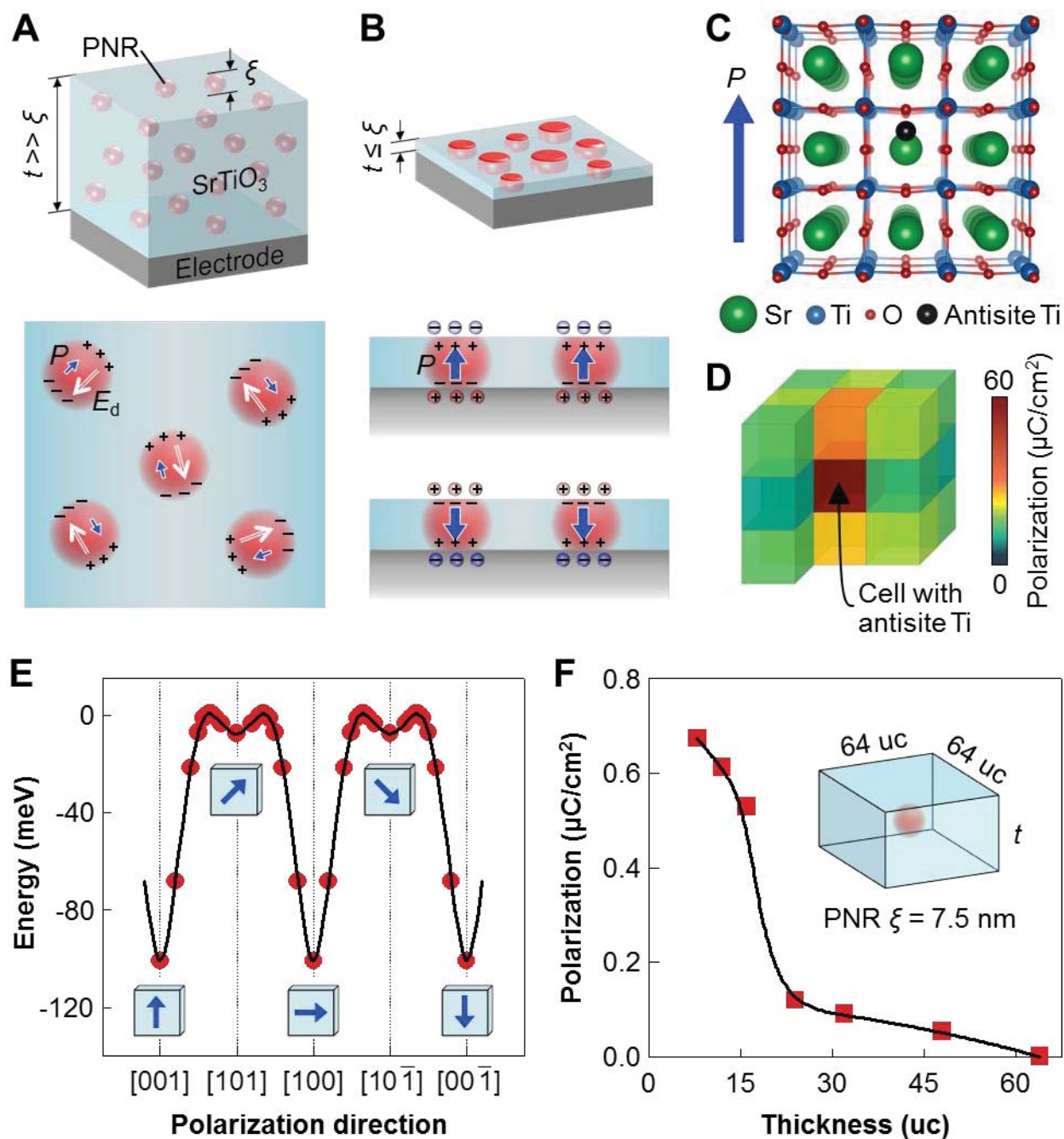
Supplementary Materials:

www.sciencemag.org

Materials and Methods

Figs. S1 to S9

References (*40–53*)

Fig. 1. **Theoretical calculations showing the emergence of ferroelectricity in ultrathin films of otherwise non-ferroelectric SrTiO₃**. (**A** and **B**) Dimensional engineering of the polarization (*P*) stability in PNRs: schematics of PNRs and their *P* in thick SrTiO₃ (**A**) and ultrathin SrTiO₃ (**B**). Blue and white arrows indicate *P* and E_d, respectively. (**C**) Calculated atomic structure near

the off-center antisite Ti atom, which induces P along the [001] (or its equivalent) direction. (**D**) Profile of local P around the antisite Ti atom in a 3×3×3 supercell obtained from DFT calculations. (**E**) Calculated energy barrier between the polarization states. Polarization switching from [001] to [00$\bar{1}$] direction can be achieved via the metastable polarization states with [101] and [10$\bar{1}$] directions. (**F**) Remnant polarization of the model system, where a single spherical PNR is embedded in SrTiO$_3$ with a thickness t, obtained by phase-field simulations. The lateral dimension of SrTiO$_3$ was fixed as 64 uc×64 uc. For details see (*23*).
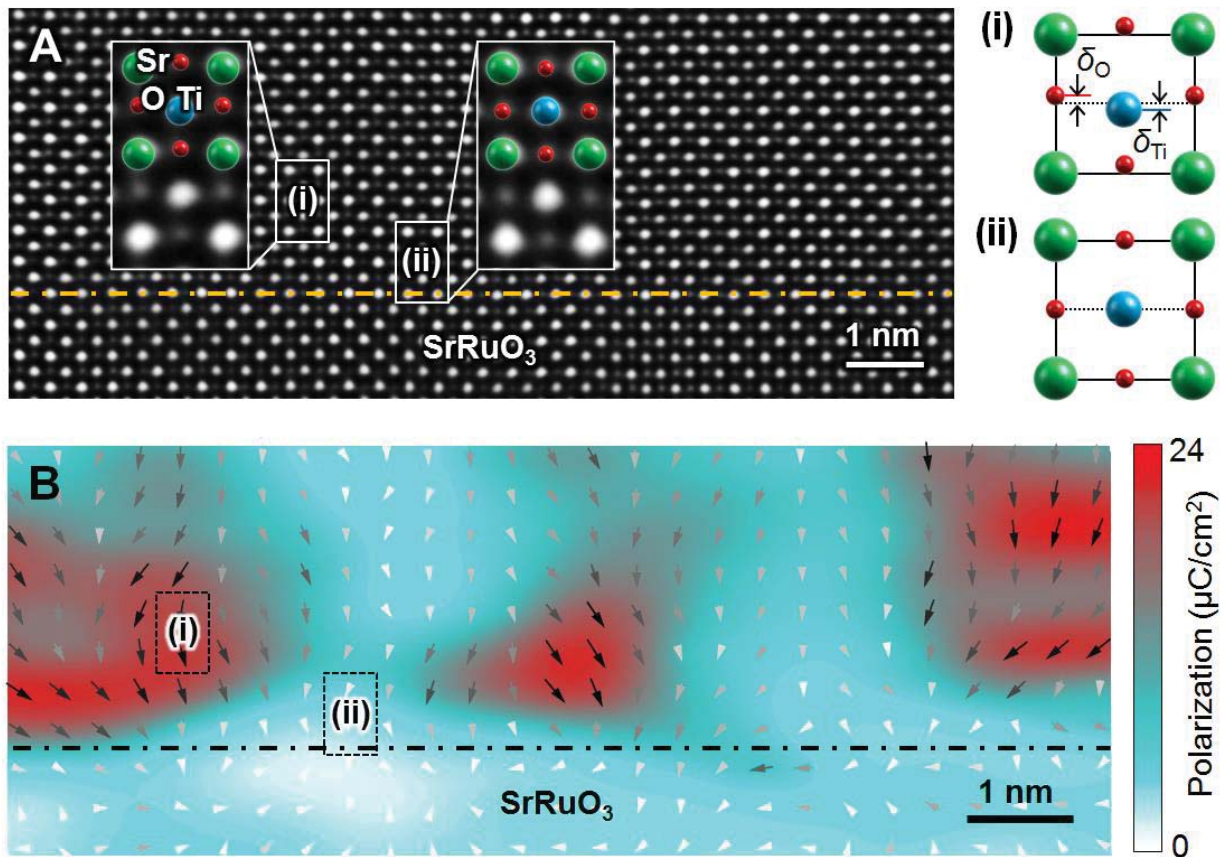
Fig. 2. Atomic-scale imaging of polar nanoregions. (**A**) Filtered ABF-STEM image, including all atomic positions. The (i) and (ii) regions are examples of polar and nonpolar regions, respectively, and are enlarged for clear view (insets). They are schematically drawn on the right; δ_{Ti} (δ_O) denotes the atomic displacement of Ti (O). (**B**) Polarization vectors for each unit cell, estimated from atomic displacements in A. Arrows denote the polarization direction; the stronger polarization, the darker the arrow color. Strength of polarization is also expressed as a color map, ranging from white (weak) to red (strong).
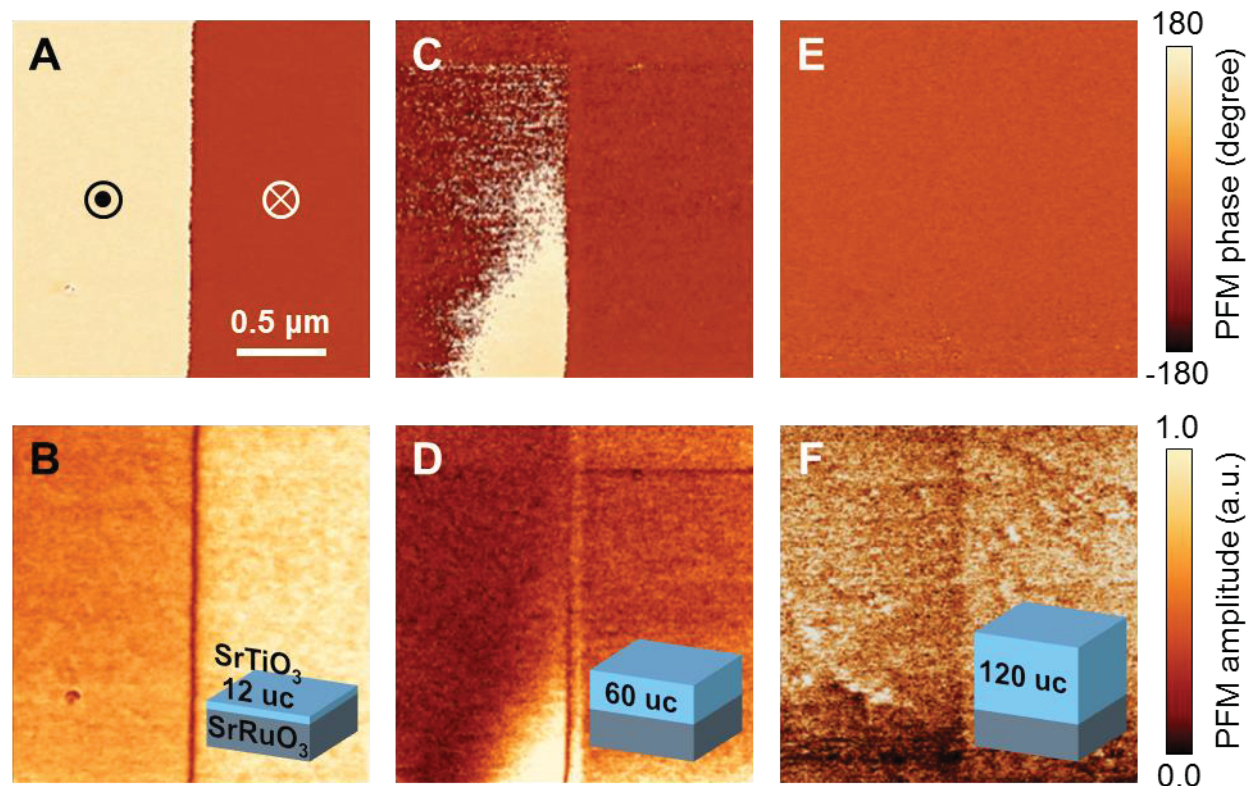
Fig. 3. Visualization of electrically-written polarization states in strain-free SrTiO$_3$ films of different thicknesses by PFM. Bipolar domain patterns of 12-uc-thick (**A** and **B**) and 60-uc-thick (**C** and **D**) SrTiO$_3$ films. The upward polarization in C and D spontaneously relaxes within several minutes. The downward polarization in C and D is characterized by a weaker amplitude PFM signal. Note that 24-uc- and 6-uc-thick SrTiO$_3$ films also show a bipolar domain pattern with clear contrast (*23*). (**E** and **F**) The thickest SrTiO$_3$ film of 120 uc does not exhibit any contrast after domain writing. The PFM amplitude signal is weak, which is consistent with the nonpolar nature of the bulk-like SrTiO$_3$ films.
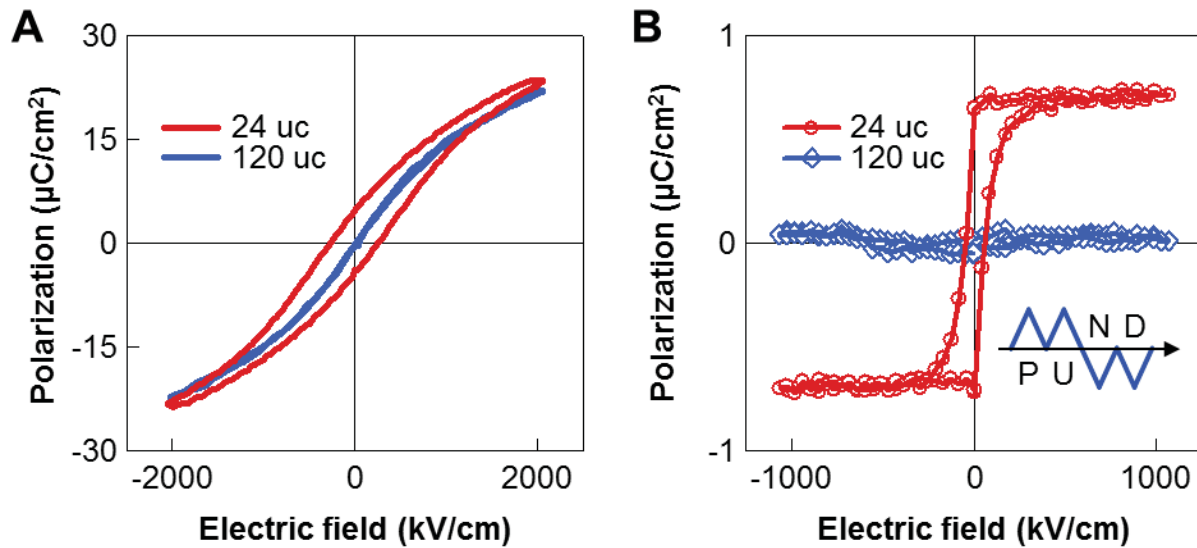
Fig. 4. Polarization hysteresis in ultrathin SrTiO$_3$ films. (**A**) Polarization versus electric field curves measured at room temperature for 24-uc- and 120-uc-thick SrTiO$_3$ films. We performed hysteresis measurements at the frequency of 20 kHz. (**B**) The polarization hysteresis of 24-uc- and 120-uc-thick SrTiO$_3$ films at room temperature, measured using the double-wave method with a triangular *ac* electric field of 10 kHz (see inset for schematic of applied waveform). We obtained the pure hysteresis component by subtracting the non-hysteresis polarization (up (U) and down (D) runs) from the total (positive (P) and negative (N) runs).

Supplementary Materials for

Emergence of Room-Temperature Ferroelectricity at Reduced Dimensions

D. Lee, H. Lu, Y. Gu, S.-Y. Choi, S.-D. Li, S. Ryu, T. R. Paudel, K. Song, E. Mikheev, S. Lee, S. Stemmer, D. A. Tenne, S. H. Oh, E. Y. Tsymbal, X. Wu, L.-Q. Chen, A. Gruverman,* C. B. Eom*

correspondence to: agruverman2@unl.edu (A.G.); eom@engr.wisc.edu (C.B.E.)

This PDF file includes:

Materials and Methods

Thin film fabrication

Strain-free $SrTiO_3$ epitaxial thin films were grown on (001) $SrTiO_3$ substrate using the pulsed laser deposition (PLD) method. Before deposition, low miscut ($< 0.05°$) $SrTiO_3$ substrates were treated with a buffered hydrofluoric acid etch and annealed in oxygen at 1050 °C for 6 hours to create atomically smooth single TiO_2 terminated surfaces with unit cell steps. A $SrRuO_3$ layer with a thickness of 10–15 nm was deposited as a bottom electrode on the $SrTiO_3$ substrate. A KrF excimer laser (248 nm) beam was focused on stoichiometric $SrRuO_3$ ceramic and $SrTiO_3$ single-crystal targets to an energy density of ~2.0 J/cm^2 and pulsed at 3–5 Hz. $SrTiO_3$ films were grown at a substrate temperature of 750 °C and oxygen partial pressures of 10 mTorr. The PLD system was equipped with high-pressure reflection high-energy electron diffraction (RHEED), which enabled atomic layer controlled growth and *in-situ* monitoring during the growth (Fig. S1). The film thickness of $SrTiO_3$ was controlled from 120 uc to 6 uc, where 1 uc corresponds to 0.3905 nm. After growth, the films were annealed in 1 atmosphere of oxygen during cooling. For the measurements of polarization–electric field ($P–E$) curves and PFM hysteresis loops, we used the additional $SrRuO_3$ layer as the top electrode. The top $SrRuO_3$ electrode was patterned by photolithography and ion-milling, with the dimensions of 50 μm in diameter and ~10 nm in thickness for $P–E$ curve measurements (or 5 μm in diameter and ~2.5 nm in thickness for PFM hysteresis loop measurements). The crystal structure of the films was determined using a high-resolution four-circle XRD machine (Bruker D8 advance; Fig. S2A). The XRD peak position of the $SrTiO_3$ film was almost identical with that of the $SrTiO_3$ substrate, indicating that our $SrTiO_3$ film had a normal unit-cell volume (with a small expansion of ≤ 0.1 %) and was free of excessive point defects. Considering the small lattice expansion, the amount of Sr deficiency in our films was expected to be at most ~1 atomic %, according to the literature (*40*). Film surfaces were imaged by AFM (Fig. S2B). Strain-free $SrTiO_3$ films were also grown as control samples using a hybrid molecular beam epitaxy (MBE) method (*41*), which was chosen for its ability to control the chemical stoichiometry of the film. This hybrid MBE approach, which combines chemical beam epitaxy and solid source MBE, is capable of growing oxide films with precise stoichiometry and atomic layer control. We used an effusion cell for Sr, an rf plasma source for oxygen, and a metal-organic source, titanium tetraisopropoxide [$Ti(OC_3H_7)_4$ or TTIP], for Ti. Growth conditions and excellent crystalline quality of the hybrid MBE-grown $SrTiO_3$ films have already been shown in detail elsewhere (*41*).

Raman spectroscopy measurements

Raman spectra were recorded using a Horiba Jobin Yvon T64000 triple spectrometer equipped with a liquid-nitrogen-cooled multichannel charge-coupled device detector. Spectra were recorded in backscattering geometry in the temperature range of 10–400 K, using a variable temperature closed cycle He cryostat. For excitation, the 325 nm He–Cd laser line was used with a power density of 0.5 W/mm^2 at the sample surface, which was low enough to avoid any noticeable local heating. Our data show the first-

order Raman peaks of $SrTiO_3$ films, denoted by the vertical dashed-dotted lines in Fig. S3A. These peaks should be forbidden in ideal paraelectric (centrosymmetric) $SrTiO_3$, and their appearance in spectra indicates that the inversion symmetry is broken, i.e., the material is polar. Note that these clear Raman peaks appear only when $SrTiO_3$ is Sr-deficient (*21*). We also measured Raman spectra for the hybrid MBE-grown $SrTiO_3$ films, which were believed to be as stoichiometric as possible. As shown in Fig. S3B, the first-order Raman peaks (denoted by dashed-dotted lines) still appeared in the hybrid MBE-grown film at low temperatures (< 100 K), similar to the $SrTiO_3$ bulk single crystals (*20*), while those became significantly weakened compared to the PLD-grown $SrTiO_3$ film. This result indicates that there is usually a small Sr deficiency (and associated PNRs), even in nominally stoichiometric $SrTiO_3$ films and single crystals.

We integrated the intensity of the first-order Raman peaks, from which we determined the nonpolar-to-polar transition temperature (Fig. S3C). We found that the first-order Raman peaks (i.e., the polar feature) persisted up to ~400 K in the PLD-grown $SrTiO_3$ film (*20*, *21*), indicating the emergence of room-temperature ferroelectricity in ultrathin $SrTiO_3$. On the other hand, in the hybrid MBE-grown $SrTiO_3$ film, the first-order Raman peaks almost disappeared at room temperature. As a result, the MBE-grown film did not reveal room-temperature ferroelectricity (Fig. S3D). These Raman spectroscopy results emphasize the possibility of tuning ferroelectricity via Sr stoichiometry in $SrTiO_3$ (especially at the ultrathin limit), as well as the intrinsic nature of Sr deficiency and associated PNRs.

Atomic-scale imaging of polarization pattern by STEM

Samples for STEM observation were prepared by mechanical grinding to a thickness of 80 μm, dimpling to a thickness of less than 10 μm, and ion-beam thinning for electron transparency. HAADF- and ABF-STEM images were taken in a STEM (JEM-2100F, JEOL, Japan) at 200 kV with a spherical aberration corrector (CEOS GmbH, Germany). The optimum size of the electron probe was 0.9 Å. The collection semi angles of the HAADF and ABF detectors ranged from 90 to 220 mrad and from 10 to 20 mrad, respectively. The obtained raw images were band-pass filtered to reduce background noise. Since the contrast difference between Sr and Ti (or Ru) atoms in the ABF-STEM image was insignificant, both HAADF- and ABF-STEM images were necessary in order to find all kinds of atomic positions. The positions of each atomic column in the STEM image were extracted by PPA (HREM Research Inc., Japan). The standard position of each unit cell was calculated from 4 neighboring Sr-atomic columns. From the obtained standard position, the positive charge position was defined by Ti-atomic columns in $SrTiO_3$ and Ru-atomic columns in $SrRuO_3$; the negative charge position was calculated by averaging the 4 oxygen atomic columns; and finally, polarization vectors from all unit cells were plotted from the negative charge center to the positve charge center. By considering the positive and negative charge positions, atomic polarization P can be simply calculated using the following equation:

$$P = \frac{1}{V}\sum_{i}\delta_i Z_i = \frac{1}{V}(\delta_{Ti}Z_{Ti} + 3\delta_O Z_O) \tag{S1}$$

where Z_i is the effective charge of i atom, δ_i is the displacement length of i atom from the standard position obtained from Sr atoms, and V is the unit cell volume (*42*). Polarization was calculated under the assumption that the displacement of invisible oxygen atoms along Ti-O atomic columns behaves identically to the other visible oxygen atoms in each unit cell. All the atomic position calculation and polarization vector plots were performed using the hand-made scripts based on MATLAB.

First-principles DFT calculations

We used the generalized gradient approximation (GGA) + U method. The Perdew-Burke-Ernzerhof (PBE) functional (*43*) is one of the most widely used functionals (*22*); however, it is known to slightly overestimate the lattice constant and bond length of solids. We chose the PBE for solids (known as PBEsol) functional, instead of PBE, to improve our calculations (*44*). We used a $3\times3\times3$ supercell containing 135 atoms. We chose Ti^{2+} and Sr^{2+} oxides as a reference state for our calculations of defect formation energy, since the antisite Ti atom has the +2 chemical valence. For barrier calculations, we considered only the transition state that is a linear mixture of initial and end states.

In order to find an energetically stable atomic structure, we considered three different local configurations for the antisite Ti atom: that is, $Ti_{OC:001}$, $Ti_{OC:011}$, and $Ti_{OC:111}$ configurations, which were defined as the off-centered antisite Ti atom (Ti_{OC}) along the [001], [011], and [111] crystalline directions, respectively. It was found that the energy gain from this Ti off-centering could be as large as ~0.5 eV, possibly originating from the structural distortion driven by ionic radii differences between Ti^{2+} (0.86 Å) and Sr^{2+} (1.44 Å). Our result showed that the $Ti_{OC:001}$ configuration is energetically favored (by ~0.1 eV) compared to the $Ti_{OC:011}$ configuration. We found that the $Ti_{OC:111}$ configuration was neither stable nor insulating. Importantly, the defect binding energy (ΔE) between Sr vacancy (V_{Sr}) and antisite Ti (Ti_{Sr}) was negative, i.e., $\Delta E = \Delta H_f (V_{Sr} + Ti_{Sr}) - \Delta H_f (V_{Sr}) - \Delta H_f (Ti_{Sr}) < 0$, indicating that the antisite Ti defect forms instantaneously in the presence of V_{Sr}, independent of growth conditions. The formation energy of Ti_{OC} was estimated to be ~1.33 eV in bulk $SrTiO_3$; however, the formation energy of Ti_{OC} can be reduced in thin films, which greatly enhances the resulting concentration of Ti_{OC}. (i) First, our calculations for the $SrTiO_3$ (10 uc)/$SrRuO_3$ (5 uc) heterostructure, which more properly reflects the real case of thin films, revealed that the formation energy of Ti_{OC} is reduced by ~0.7 eV (on the surface or in the middle of the $SrTiO_3$ layer) and ~1.6 eV (at the $SrTiO_3$/$SrRuO_3$ interface), compared to that in $SrTiO_3$ bulk (Fig. S4A). The octahedral rotation and tilt in $SrRuO_3$ were explicitly taken into account using a $\sqrt{2}\times\sqrt{2}\times2$ pseudo-cubic lattice with the in-plane lattice constant fixed to the experimental lattice constant of $SrTiO_3$. All other parameters were explicitly relaxed. Considering the layer-by-layer growth process (schematically drawn in Fig. S4B), the formation energy of Ti_{OC} would follow these reduced values rather than the bulk value. (ii) Thin-film growth is a non-equilibrium kinetic process. Such a non-equilibrium growth condition can lead to a higher number of defects in thin films than in bulk (*45*). (iii) Point defects tend to agglomerate and form clusters. Such clustering can increase the local concentration of Ti_{OC}.

For the $Ti_{OC:001}$ configuration, it was found that the antisite Ti atom had a large off-centering of around 0.8 Å. Energy barriers have been calculated as 102 meV and 8 meV for the switching of $Ti_{OC:001} \rightarrow Ti_{OC:011}$ and $Ti_{OC:011} \rightarrow Ti_{OC:001}$, respectively (Fig. 1E), which are comparable to the energy barrier of ~100 meV in conventional ferroelectric $PbTiO_3$ (*24*). On the other hand, for the direct switching of $Ti_{OC:001} \rightarrow Ti_{OC:00-1}$, the calculated energy barrier is 501 meV, which is rather large for the polarization switching.

The total dipole moment of the supercell is calculated with the formula below:

$$p = \sum_{all\ atoms} (\frac{\partial p}{\partial r} \cdot dr) \tag{S2}$$

where $\partial p/\partial r$ denotes the born effective charge (known as Z*, varied by atom), which is calculated using the density functional perturbation theory (*46, 47*), and dr is the displacement of the atom from the position of polarization-free bulk $SrTiO_3$. The calculated local polarization profile (Fig. 1D) shows that the antisite Ti atom not only induces a local polarization as large as 55 $\mu C/cm^2$ in its residing unit cell, but also causes other surrounding cells to be coherently polarized. The overall average P of the supercell is estimated as ~17 $\mu C/cm^2$. The contribution of the dipole moment from the unit cell of the antisite Ti atom is only 12.1 % (or 12.8%) of the total 16.96 (or 14.85) $e \cdot$Å for the $Ti_{OC:001}$ (or $Ti_{OC:011}$) configuration. In other words, despite the large off-centering of the antisite Ti atom (as large as 0.8 Å), its localized dipole moment is not very large, due to its low Born effective charge (1.57 for Ti^{2+} compared to 7.02 for Ti^{4+} in the $Ti_{OC:001}$ configuration). Thus, the overall dipole moment is dominated by the induced dipole moments, not merely by the off-centering of the antisite Ti atom itself.

Phase-field simulations

In our phase-field model, the temporal evolution of the three-dimensional polarization field (P_i, $i = 1, 2, 3$) is described by the time-dependent Ginzburg-Landau (TDGL) equation:

$$\frac{\partial P_i(\boldsymbol{x},t)}{\partial t} = -L\frac{\delta F}{\delta P_i(\boldsymbol{x},t)}, \quad (i = 1, 2, 3) \tag{S3}$$

where $\boldsymbol{x}$ is the spatial position in the Cartesian coordinate system and L is the kinetic relaxation coefficient related to the domain wall mobility. The TDGL is solved numerically using the semi-implicit Fourier spectral method (*48*). The total free energy F in Eq. (S3) includes all the relevant energetic contributions as seen below:

$$F = \int_V (f_{bulk} + f_{grad.} + f_{elas.} + f_{elec.})dV \tag{S4}$$

where f_{bulk}, $f_{grad.}$, $f_{elas.}$, and $f_{elec.}$ are the bulk, gradient, elastic, and electrostatic contributions, respectively. The phenomenological potential and parameters of $SrTiO_3$ were taken from Li *et al.* (*49*). The potential of PNR has a similar form as that of $SrTiO_3$, except for the Landau-Devonshire coefficients, which were modified to make sure that the spontaneous polarization of PNR is $P_1 = 0.1$ C/m^2 and $P_2 = P_3 = 0$ at room temperature.

The discretized three dimensional simulation size was $64\Delta x \times 64\Delta x \times 64\Delta x$, with a grid spacing of $\Delta x = 0.39$ nm. The PNR with a diameter of 7.5 nm was placed in the center of the $SrTiO_3$ bulk/film. For the bulk simulation (i.e., $64\Delta x$), periodic boundary conditions were imposed in all three directions. For the thin film simulations, periodic boundary conditions were applied along the x_1 and x_2 axes. Along the x_3 direction, the system was divided into three parts: air, thin film, and substrate. Thin film thicknesses were taken to be $8\Delta x$, $12\Delta x$, $16\Delta x$, $24\Delta x$, $32\Delta x$, and $48\Delta x$. All the simulations were conducted under strain-free boundary conditions ($\varepsilon_{ij} = 0$). For thin films, a mixed boundary condition was applied as well, i.e., the displacement at the bottom of the substrate was assumed to be zero, and the stress components along x_3 directions (σ_{i3}) were all zero on the top surface of the thin film (*50*). Following Khachaturyan's micro-elasticity theory (*51*), local stress and strain were calculated from the mechanical equilibrium condition:

$$\frac{\partial \sigma_{ij}}{\partial x_j} = 0, \qquad (i, j = 1, 2, 3) \qquad\qquad (S5)$$

where σ_{ij} are the stress tensor components. We chose a short-circuit electric boundary condition for both bulk and thin film simulations (*52*). In order to consider the total compensation of the surface charge, the electric potential of both the top surface and the bottom of the thin film were set to zero. The system was first subjected to an electric field of 5×10^6 V/m for 40,000 steps to reach equilibrium. Then the electric field was removed and the system was relaxed to equilibrium (after 40,000 steps) in order to obtain the remnant polarization of the system (Fig. 1F).

PFM measurements

Nanoscale polarization imaging and local switching spectroscopy were performed using a resonant-enhanced piezoresponse force microscopy (MFP-3D, Asylum Research). Conductive silicon cantilevers (PPP-EFM, Nanosensors) were used in this study. Tip contact forces were calibrated by measuring the force-distance curves. Bipolar domain patterns have been created in the $SrTiO_3$ films with a thickness of less than 60 uc by scanning the film surface with an electrically-biased PFM tip (Fig. 3 and Fig. S5).

The as-grown region of the ultrathin $SrTiO_3$ films (denoted by (a) in Fig. S6) was weakly polarized downward, which may have been due to the intrinsic contribution from downward irreversible surface dipoles (*53*). As shown in Fig. S6, after the bipolar domain pattern was electrically written (denoted by a blue dotted-line frame, i.e., the (b) region), the center region (denoted by a yellow dotted-line frame, i.e., the (c) region) was scanned with the electrically grounded tip under an incrementally increasing loading force. The loading force was increased in the bottom-up direction (denoted by a black arrow) from 100 to 1000 nN. We found that the tip-induced strain gradient could reverse the polarization state in our ultrathin $SrTiO_3$ film from upward to downward, without any electrical bias, which can be explained by the intrinsic coupling between polarization and strain gradient via flexoelectricity (*32*).

PFM hysteresis loops were obtained by measuring the PFM signal as a function of the switching pulse amplitude (pulse duration was 25 ms) superimposed on an *ac* modulation bias with an amplitude of 0.8 V_{p-p} at 320 kHz. Significantly, we observed a

clear PFM hysteresis loop in the ultrathin $SrTiO_3$ capacitor as well as on the bare $SrTiO_3$ film surface (Fig. S7A). From this result, we were able to exclude the electrostatic tip-sample interaction effects for the observed PFM response, since electrostatic forces are typically too small in the capacitor geometry. We also systematically explored how the piezoresponse signal depends on a mechanical stress. Due to the coupling between polarization and strain gradient known as the flexoelectric effect, the strain gradient can break the equilibrium between the two polarization states in ferroelectrics and even reverse the polarization state (*32*). An AFM tip can effectively generate a local strain gradient and a downward flexoelectric field near the film surface, whose magnitude is controlled by varying the tip loading force. Figure S7B shows the PFM hysteresis loops of our ultrathin $SrTiO_3$ film as a function of the loading force, clearly representing the coupling between polarization and strain gradient: the increased loading force (from 20 to 500 nN) makes the piezoelectric loop much more asymmetric, which means that downward polarization becomes more favored by the increased strain gradient.

We found that 12-uc-thick $SrTiO_3$ film has a stable polarization state that can be sustained for at least several hours (Fig. S8). We examined the gradual decay of the PFM signals (Fig. S8B) and found that the switched polarization states of 12-uc-thick $SrTiO_3$ film could be stable for at least several hours, while those of 120-uc-thick $SrTiO_3$ disappeared in a few seconds. The polarization relaxation usually follows the power-law decay, $P(t) \propto t^{-\alpha}$, where α is the decay exponent. The smaller α value generally corresponds to the higher stability of polarization. Referring to the α values, the stability of polarization ($\alpha = 0.14$) of 12-uc-thick strain-free $SrTiO_3$ film seems as good as that ($\alpha = 0.12$) of a conventional ferroelectric 12-uc-thick (001) $BaTiO_3$ film on $SrRuO_3/SrTiO_3$ substrate (with a compressive strain of 2.2%) and much better than that ($\alpha = 0.21$) of a 50-nm-thick strained (001) $SrTiO_3$ film (with a compressive strain of 1.2%) on (110) $NdGaO_3$ substrate (*20*).

We also explored the temperature dependence of the PFM response. Considering the Raman spectroscopy data (Fig. S3C) and the intrinsic contribution from the downward surface dipoles (*53*), we were able to roughly predict the double-well potential of polarization states of ultrathin $SrTiO_3$ films, as schematically drawn in Fig. S9A. From the variable-temperature PFM measurements (Fig. S9B), we found that the upward polarization state became unstable as the temperature was elevated above 350 K, while the downward polarization state remained rather stable, in agreement with our prediction.
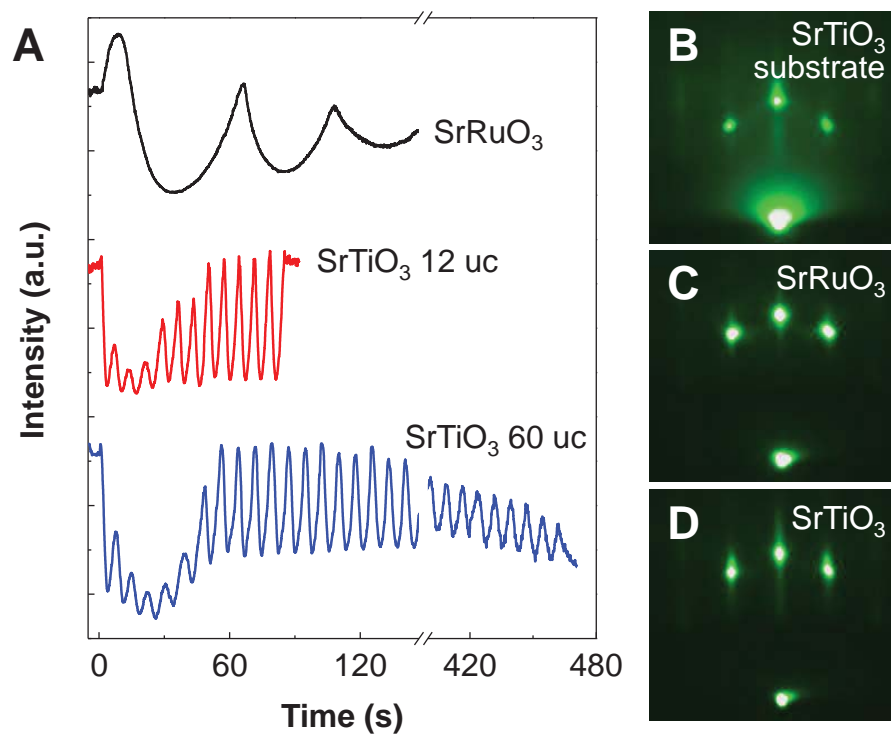
Fig. S1. Film growth. (**A**) RHEED intensity oscillations during growth of SrRuO$_3$ film on SrTiO$_3$ substrate and SrTiO$_3$ film on SrRuO$_3$/SrTiO$_3$ substrate. (**B** to **D**) Typical RHEED patterns of the SrTiO$_3$ substrate (**B**), SrRuO$_3$ layer on SrTiO$_3$ (**C**), and SrTiO$_3$ layer on SrRuO$_3$/SrTiO$_3$ (**D**).
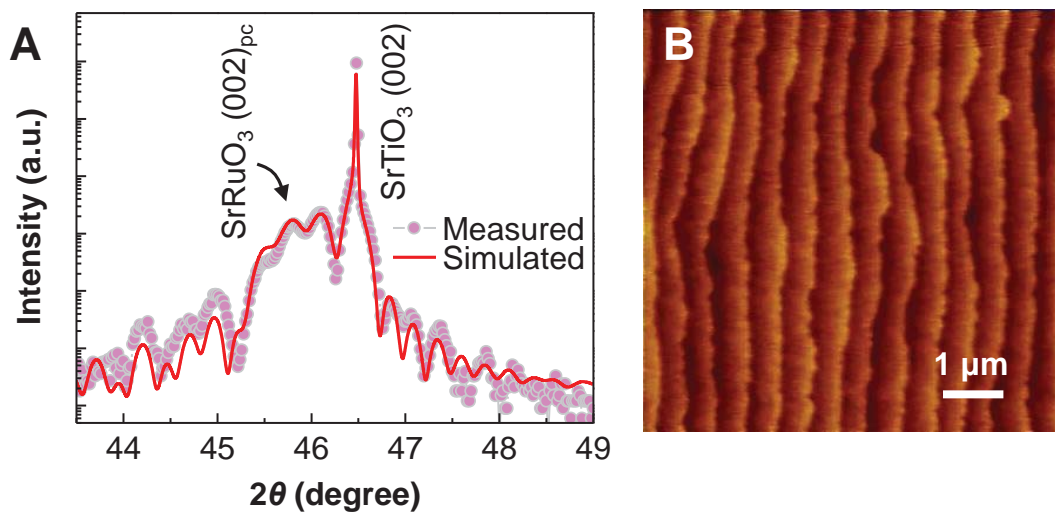
Fig. S2. Structural characterization. (**A**) Measured and simulated XRD θ-2θ curves for $SrTiO_3$ film on $SrRuO_3$/$SrTiO_3$ substrate. The $SrTiO_3$ and $SrRuO_3$ layers were 57-uc- and ~15-nm-thick, respectively. The peak position of the $SrTiO_3$ film was almost identical with that of the $SrTiO_3$ substrate. This indicates that our $SrTiO_3$ film had a normal unit-cell volume and was free of excessive point defects. (**B**) AFM image of the $SrTiO_3$ film, which shows the atomically smooth film surface.
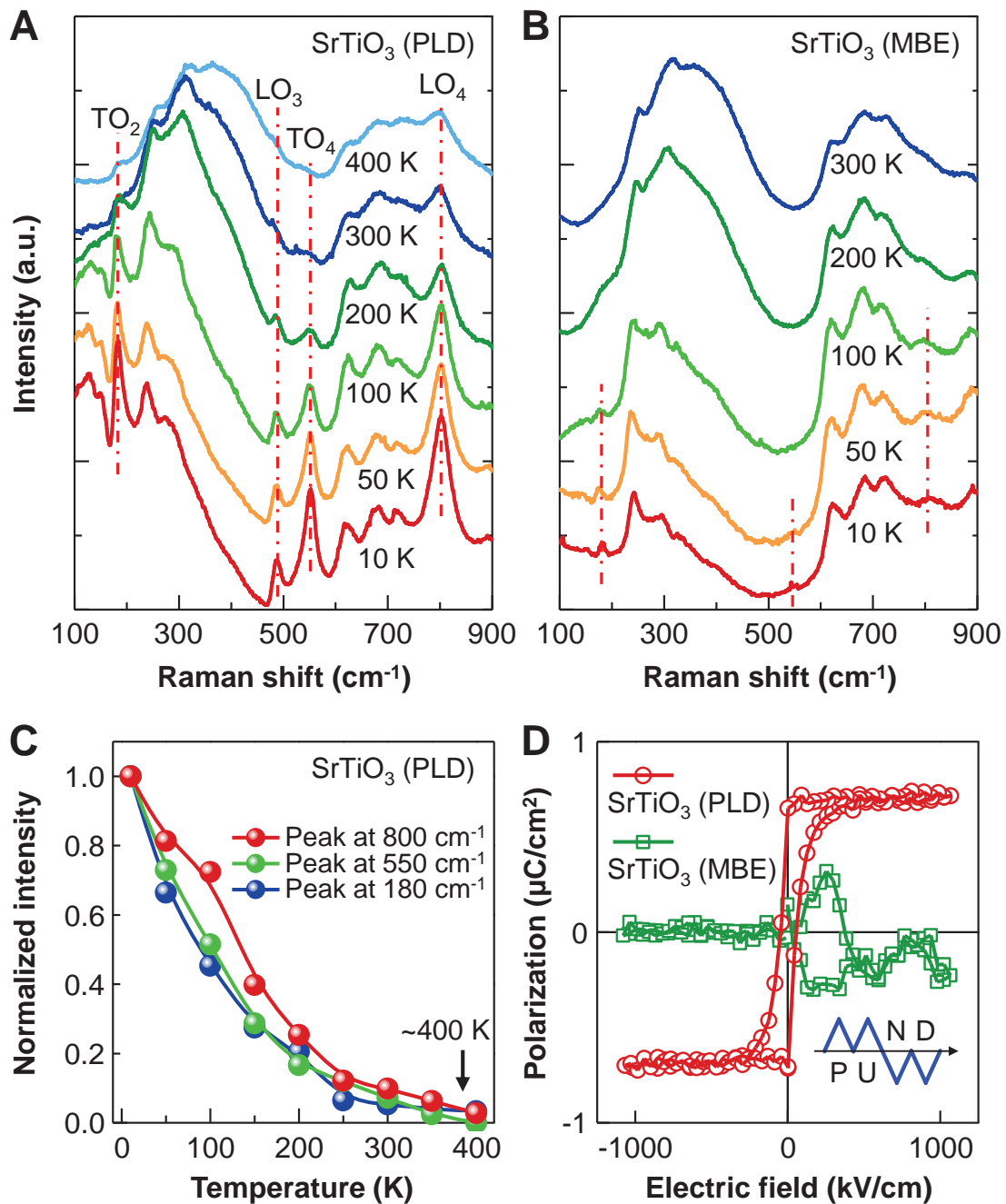
Fig. S3. Ferroelectricity in ultrathin SrTiO₃ films by Sr deficiency and associated PNRs. (**A** and **B**) Variable-temperature Raman spectra of SrTiO₃ films on SrTiO₃ substrate, grown using the PLD (**A**) and hybrid MBE method (**B**). The PLD-grown SrTiO₃ film clearly shows the first-order phonon peaks, guided by the vertical dashed-dotted lines, while the hybrid MBE-grown SrTiO₃ film shows significantly weakened first-order peaks. (**C**) Integrated intensity for the first-order Raman peaks in the PLD-grown SrTiO₃ film as a function of temperature. The first-order Raman peaks were found to persist up to ~400 K, although their intensity was reduced at high temperatures. From

this temperature-dependent result, the nonpolar-to-polar transition temperature was roughly estimated as ~400 K (*20*, *21*). (**D**) The polarization hysteresis of 24-uc-thick SrTiO$_3$ films was measured using the double-wave method with a triangular *ac* electric field of 10 kHz (see inset for schematic of applied waveform). The pure hysteresis component was obtained by subtracting the non-hysteresis polarization (up (U) and down (D) runs) from the total (positive (P) and negative (N) runs). The PLD-grown SrTiO$_3$ film (24 uc) showed a ferroelectric feature with nonzero remnant polarization, while the hybrid MBE-grown SrTiO$_3$ film (24 uc) showed no room-temperature ferroelectricity.
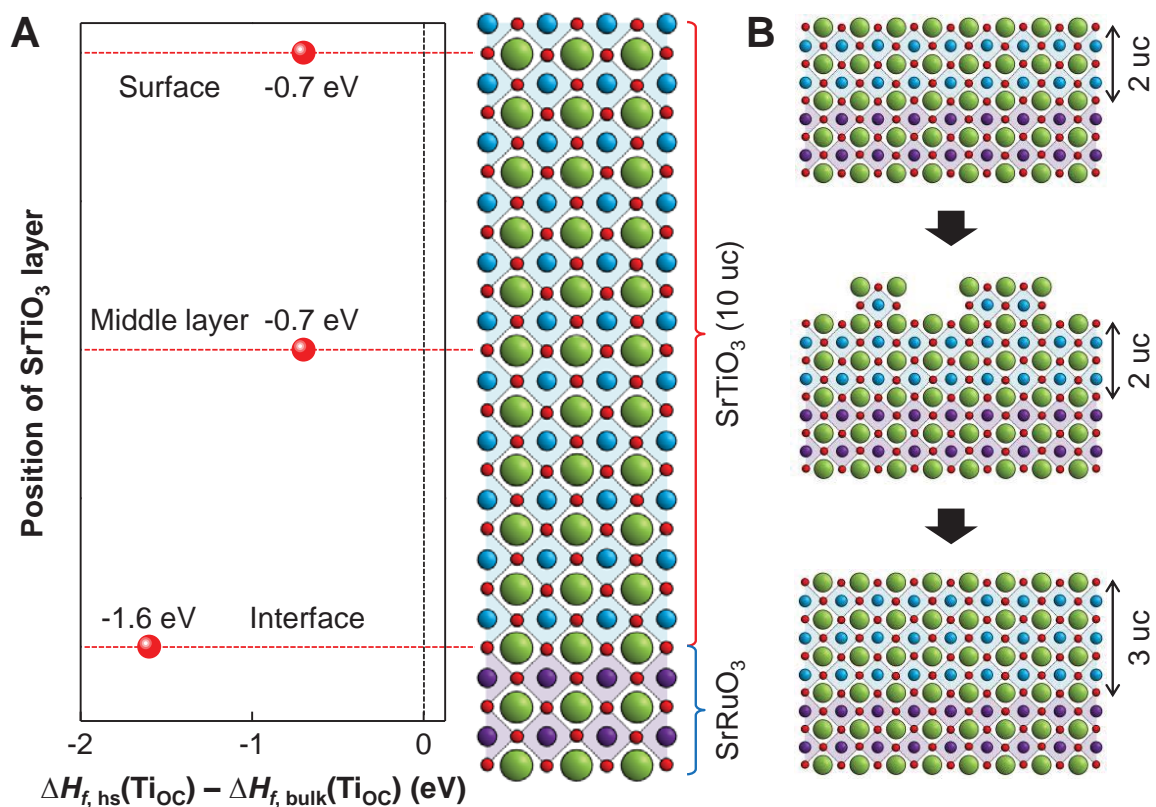
Fig. S4. Formation of off-centered antisite Ti atoms (Ti_{OC}) in $SrTiO_3$/$SrRuO_3$ heterostructures. (**A**) The formation energies of Ti_{OC} in a $SrTiO_3$/$SrRuO_3$ heterostructure ($\Delta H_{f, hs}(Ti_{OC})$) and $SrTiO_3$ bulk ($\Delta H_{f, bulk}(Ti_{OC})$), according to the position of the $SrTiO_3$ layer. (**B**) Schematic drawing of the layer-by-layer growth process of $SrTiO_3$ thin films.
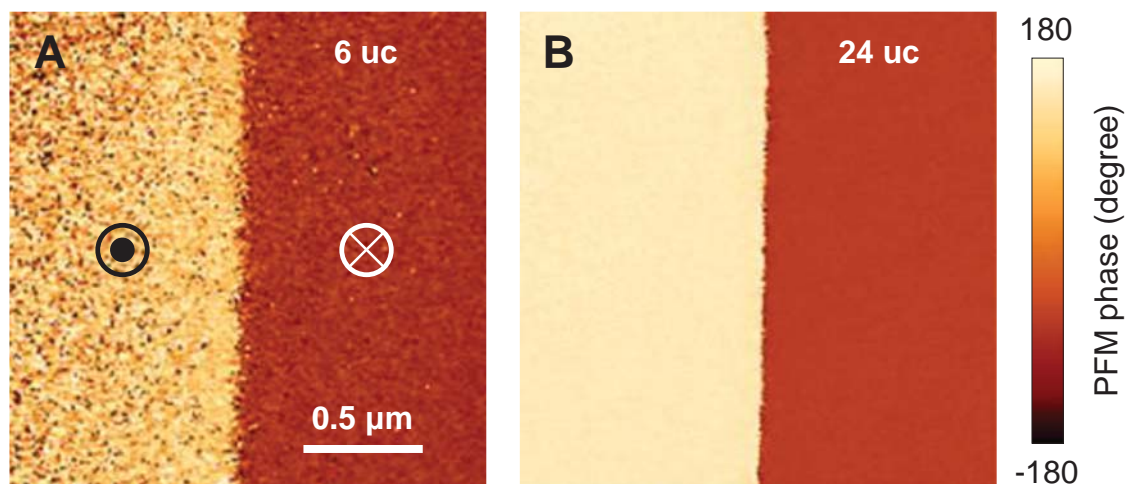
Fig. S5. Electrically written bipolar domain pattern in SrTiO₃ films. PFM phase images of 6-uc-thick (**A**) and 24-uc-thick (**B**) SrTiO₃ films.
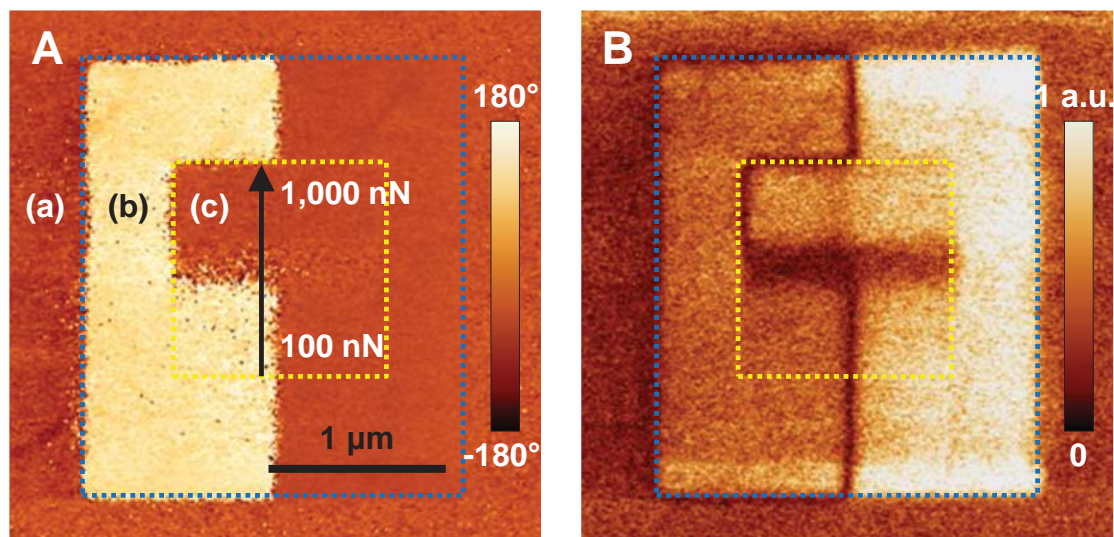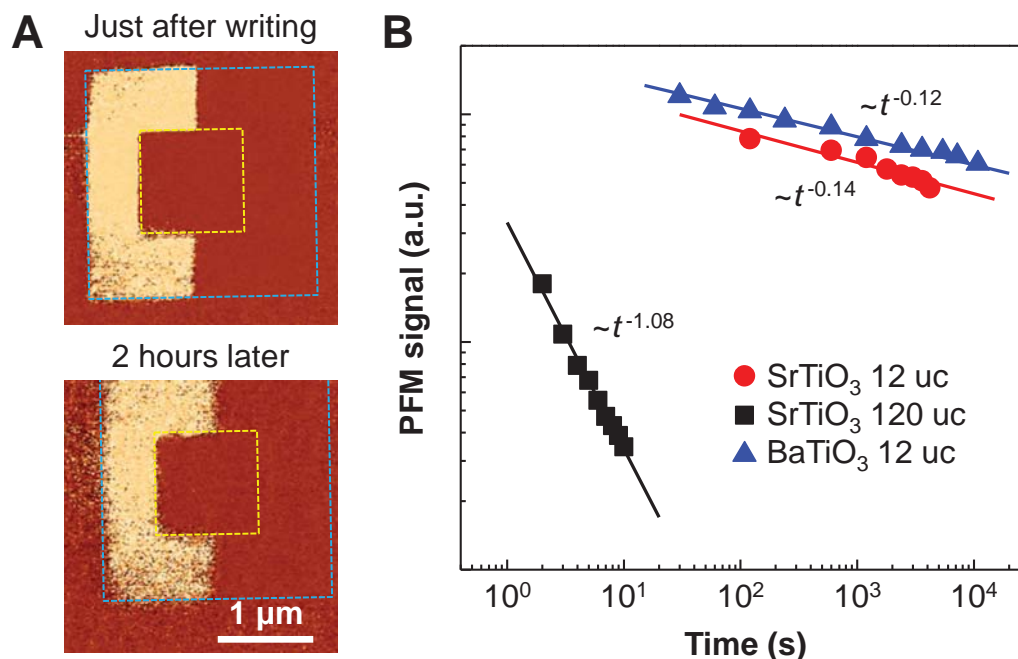
Fig. S6. Mechanical switching of ferroelectric polarization. PFM phase (**A**) and amplitude (**B**) image for the 3×3 μm^2 area of 12-uc-thick $SrTiO_3$ film. The images include the as-grown (a), electrically written (b), and mechanically written (c) regions. The as-grown region was weakly polarized downward, consistent with the STEM result (Fig. 2).
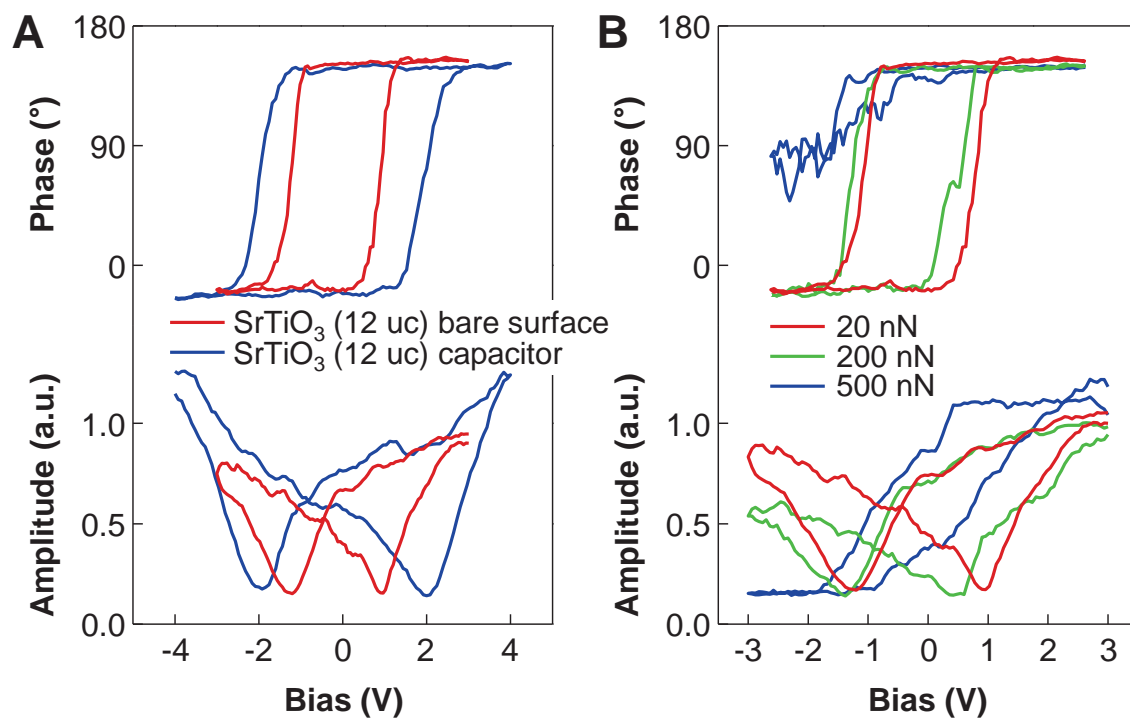
**Fig. S7. PFM hysteresis loops.** (**A**) PFM phase and amplitude hysteresis loops measured for the 12-uc-thick $SrTiO_3$ film. (**B**) PFM phase and amplitude hysteresis loops measured for the 12-uc-thick $SrTiO_3$ film, as a function of tip loading force.

A Just after writing

B

2 hours later

1 μm

PFM signal (a.u.)

$\sim t^{-0.12}$

$\sim t^{-0.14}$

$\sim t^{-1.08}$

● SrTiO₃ 12 uc
■ SrTiO₃ 120 uc
▲ BaTiO₃ 12 uc

Time (s)

Fig. S8. Stability of polarization states, examined by PFM. (**A**) PFM phase images for the 12-uc-thick $SrTiO_3$ film, measured just after the domain patterning (upper panel) and 2 hours later (lower panel). (**B**) PFM signal measured at room temperature, as a function of time after poling the (12-uc- and 120-uc-thick) $SrTiO_3$ and (12-uc-thick) $BaTiO_3$ films. Solid lines are fit to the power-law decay, $P(t) \propto t^{-\alpha}$, where α is the decay exponent. Referring to the α values, the stability of polarization ($\alpha = 0.14$) of 12-uc-thick $SrTiO_3$ film seemed as good as that ($\alpha = 0.12$) of a conventional ferroelectric 12-uc-thick $BaTiO_3$ film (with a compressive strain of 2.2%).
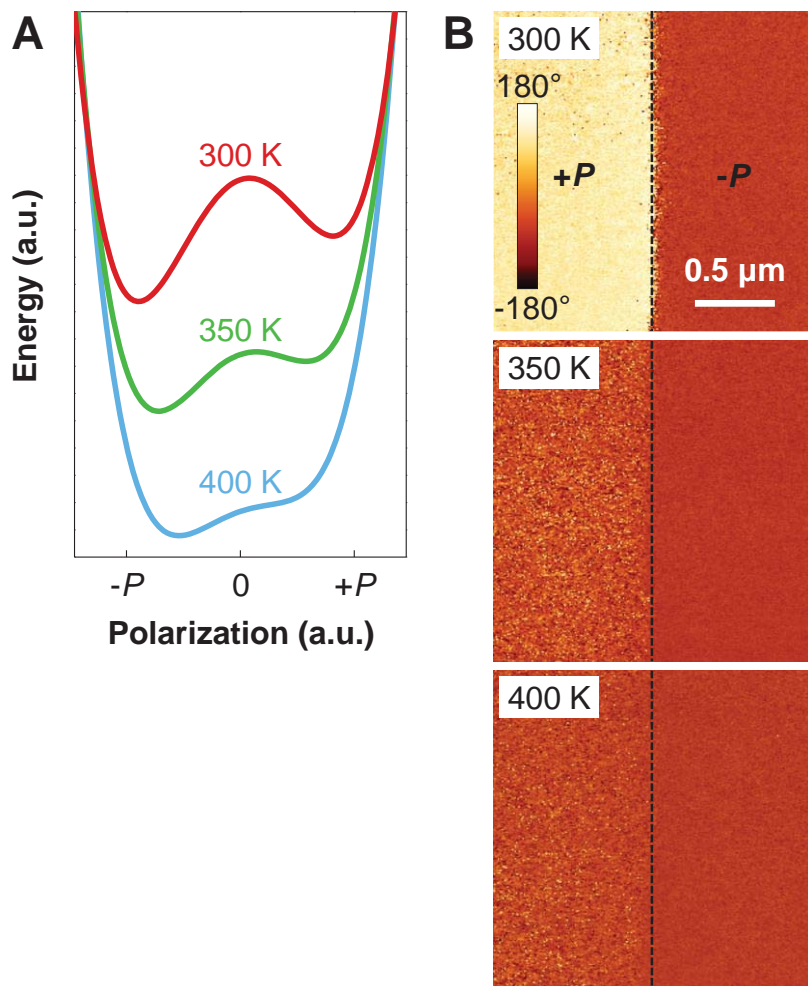
Fig. S9. Variable-temperature PFM measurement. (**A**) Schematic drawing of the predicted double-well potentials of polarization states in ultrathin SrTiO$_3$ films, at the elevated temperatures. (**B**) PFM phase images for the 12-uc-thick SrTiO$_3$ film, measured at room temperature and at elevated temperatures.

References and Notes

1. C. H. Ahn, K. M. Rabe, J.-M. Triscone, Ferroelectricity at the nanoscale: local polarization in oxide thin films and heterostructures. *Science* **303**, 488–491 (2004).

2. J. F. Scott, C. A. Paz de Araujo, Ferroelectric memories. *Science* **246**, 1400–1405 (1989).

3. M. Y. Zhuravlev, R. F. Sabirianov, S. S. Jaswal, E. Y. Tsymbal, Giant electroresistance in ferroelectric tunnel junctions. *Phys. Rev. Lett.* **94**, 246802 (2005).

4. V. Garcia *et al.*, Giant tunnel electroresistance for non-destructive readout of ferroelectric states. *Nature* **460**, 81–84 (2009).

5. A. Gruverman *et al.*, Tunneling electroresistance effect in ferroelectric tunnel junctions at the nanoscale. *Nano Lett.* **9**, 3539−3543 (2009).

6. V. Garcia *et al.*, Ferroelectric control of spin polarization. *Science* **327**, 1106–1110 (2010).

7. D. Pantel, S. Goetze, D. Hesse, M. Alexe, Reversible electrical switching of spin polarization in multiferroic tunnel junctions. *Nat. Mater.* **11**, 289–293 (2012).

8. E. Durgun, P. Ghosez, R. Shaltaf, X. Gonze, J.-Y. Raty, Polarization vortices in germanium telluride nanoplatelets: A theoretical study. *Phys. Rev. Lett.* **103**, 247601 (2009).

9. J. Mannhart, D. G. Schlom, Oxide interfaces—an opportunity for electronics. *Science* **327**, 1607–1611 (2010).

10. W. L. Zhong, Y. G. Wang, P. L. Zhang, B. D. Qu, Phenomenological study of the size effect on phase transitions in ferroelectric particles. *Phys. Rev. B* **50**, 698–703 (1994).

11. J. Junquera, Ph. Ghosez, Critical thickness for ferroelectricity in perovskite ultrathin films. *Nature* **422**, 506–509 (2003).

12. C. Lichtensteiger, J.-M. Triscone, J. Junquera, Ph. Ghosez, Ferroelectricity and tetragonality in ultrathin $PbTiO_3$ films. *Phys. Rev. Lett.* **94**, 047603 (2005).

13. H. Lu *et al.*, Enhancement of ferroelectric polarization stability by interface engineering. *Adv. Mater.* **24**, 1209–1216 (2012).

14. M. Stengel, D. Vanderbilt, N. A. Spaldin, Enhancement of ferroelectricity at metal–oxide interfaces. *Nat. Mater.* **8**, 392–397 (2009).

15. G. Burns, F. H. Dacol, Crystalline ferroelectrics with glassy polarization behavior. *Phys. Rev. B* **28**, 2527–2530 (1983).

16. L. E. Cross, Relaxor ferroelectrics. *Ferroelectrics* **76**, 241–267 (1987).

17. N. W. Ashcroft, N. D. Mermin, *Solid State Physics* (Holt, Rinehart and Winston, New York, 1976).

18. K. R. Udayakumar, A. N. Cormack, Non-stoichiometry in alkaline earth excess alkaline earth titanate. *J. Phys. Chem. Solids* **50**, 55–60 (1989).

19. B. Liu *et al.*, Composition dependent intrinsic defect structures in $SrTiO_3$. *Phys. Chem. Chem. Solids* **16**, 15590–15596 (2014).

20. H. W. Jang *et al.*, Ferroelectricity in strain-free $SrTiO_3$ thin films. *Phys. Rev. Lett.* **104**, 197601 (2010).

21. D. A. Tenne *et al.*, Ferroelectricity in nonstoichiometric $SrTiO_3$ films studied by ultraviolet Raman spectroscopy. *Appl. Phys. Lett.* **97**, 142901 (2010).

22. M. Choi, F. Oba, I. Tanaka, Role of Ti antisitelike defects in $SrTiO_3$. *Phys. Rev. Lett.* **103**, 185502 (2009).

23. Supplementary materials are available on *Science* Online.

24. R. E. Cohen, Origin of ferroelectricity in perovskite oxides. *Nature* **358**, 136–138 (1992).

25. K. A. Müller, H. Bukard, $SrTiO_3$: An intrinsic quantum paraelectric below 4 K. *Phys. Rev. B* **19**, 3593–3602 (1979).

26. J. H. Haeni *et al.*, Room-temperature ferroelectricity in strained $SrTiO_3$. *Nature* **430**, 758–761 (2004).

27. M. P. Warusawithana *et al.*, A ferroelectric oxide made directly on silicon. *Science* **324**, 367–370 (2009).

28. K. J. Choi *et al.*, Enhancement of ferroelectricity in strained $BaTiO_3$ thin films. *Science* **306**, 1005–1009 (2004).

29. C. B. Eom *et al.*, Single-crystal epitaxial thin films of the isotropic metallic oxides $Sr_{1-x}Ca_xRuO_3$. *Science* **258**, 1766–1769 (1992).

30. K. W. Urban, Studying atomic structures by aberration-corrected transmission electron microscopy. *Science* **321**, 506–510 (2008).

31. R. Ishikawa *et al.*, Direct imaging of hydrogen-atom columns in a crystal by annular bright-field electron microscopy. *Nat. Mater.* **10**, 278–281 (2011).

32. H. Lu *et al.*, Mechanical writing of ferroelectric polarization. *Science* **336**, 59–61 (2012).

33. J. F. Scott *et al.*, Switching kinetics of lead zirconate titanate submicron thin-film memories. *J. Appl. Phys.* **64**, 787–792 (1988).

34. A. Ohtomo, H. Y. Hwang, A high-mobility electron gas at the $LaAlO_3/SrTiO_3$ heterointerface. *Nature* **427**, 423–426 (2004).

35. N. Reyren *et al.*, Superconducting interfaces between insulating oxides. *Science* **317**, 1196–1199 (2007).

36. A. Brinkman *et al.*, Magnetic effects at the interface between non-magnetic oxides. *Nat. Mater.* **6**, 493–496 (2007).

37. U. Bianchi, J. Dec, W. Kleemann, J. G. Bednorz, Cluster and domain-state dynamics of ferroelectric $Sr_{1-x}Ca_xTiO_3$ ($x = 0.007$). *Phys. Rev. B* **51**, 8737–8746 (1995).

38. D. A. Tenne *et al.*, Probing nanoscale ferroelectricity by ultraviolet Raman spectroscopy. *Science* **313**, 1614–1616 (2006).

39. A. T. Bollinger *et al.*, Superconductor-insulator transition in $La_{2-x}Sr_xCuO_4$ at the pair quantum resistance. *Nature* **472**, 458–460 (2011).

40. T. Ohnishi, K. Shibuya, T. Yamamoto, M. Lippmaa, Defects and transport in complex oxide thin films. *J. Appl. Phys.* **103**, 103703 (2008).

41. J. Son *et al.*, Epitaxial $SrTiO_3$ films with electron mobilities exceeding 30,000 cm^2 V^{-1} s^{-1}. *Nat. Mater.* **9**, 482–484 (2010).

42. C.-L. Jia *et al.*, Unit-cell scale mapping of ferroelectricity and tetragonality in epitaxial ultrathin ferroelectric films. *Nat. Mater.* **6**, 64–69 (2007).

43. J. P. Perdew, K. Burke, M. Ernzerhof, Generalized gradient approximation made simple. *Phys. Rev. Lett.* **77**, 3865–3868(1996).

44. J. P. Perdew *et al.*, Restoring the density-gradient expansion for exchange in solids and surfaces. *Phys. Rev. Lett.* **100**, 136406 (2008).

45. J. D. Perkins *et al.*, Inverse design approach to hole doping in ternary oxides: Enhancing *p*-type conductivity in cobalt oxide spinels. *Phys. Rev. B* **84**, 205207 (2011).

46. R. D. King-Smith, D. Vanderbilt, *Phys. Rev. B* **47**, 1651–1654 (1993).

47. R. Resta, *Rev. Mod. Phys.* **66**, 899–915 (1994).

48. L. Q. Chen, J. Shen, Applications of semi-implicit Fourier-spectral method to phase field equations. *Comput. Phys. Commun.* **108**, 147–158 (1998).

49. Y. L. Li *et al.*, Phase transitions and domain structures in strained pseudocubic (100) $SrTiO_3$ thin films. *Phys. Rev. B* **73**, 184112 (2006).

50. Y. L. Li, S. Y. Hu, Z. K. Liu, L. Q. Chen, Effect of substrate constraint on the stability and evolution of ferroelectric domain structures in thin films. *Acta Mater.* **50**, 395–411 (2002).

51. A. G. Khachaturyan, *Theory of Structural Transformations in Solids* (DOVER PUBLICATIONS INC. Mineola, New York, 2008).

52. Y. L. Li, S. Y. Hu, Z. K. Liu, L. Q. Chen, Effect of electrical boundary conditions on ferroelectric domain structures in thin films. *Appl. Phys. Lett.* **81**, 427–429 (2002).

53. R. I. Eglitis, D. Vanderbilt, First-principles calculations of atomic and electronic structure of $SrTiO_3$ (001) and (011) surfaces. *Phys. Rev. B* **77**, 195408 (2008).